

The automatic gain-matching in the PIBETA CsI calorimeter

E. Frlež^{a,1}, M. Bychkov^a, and D. Počanić^a

^a *Department of Physics, University of Virginia, Charlottesville, VA 22904, USA*

Segmented electromagnetic calorimeters are used to determine both the total energy and direction (momentum components) of charged particles and photons. A trade off is involved in selecting the degree of segmentation of the calorimeter as the spatial and energy resolutions are affected differently. Increased number of individual detectors reduces accidental particle pile-up per detector but introduces complications related to ADC pedestals and pedestal variations, exacerbates the effects of electronic noise and ground loops, and requires summing and discrimination of multiple analog signals. Moreover, electromagnetic showers initiated by individual ionizing particles spread over several detectors. This complicates the precise gain-matching of the detector elements which requires an iterative procedure. The PIBETA calorimeter is a 240-module pure CsI non-magnetic detector optimized for detection of photons and electrons in the energy range 5–100 MeV. We present the computer-controlled, automatic, in situ gain-matching procedure that we developed and used routinely in several rare pion and muon decay experiments with the PIBETA detector.

PACS Numbers: 29.40.Gx, 29.40.Vj, 29.85.+c

Keywords: Large acceptance segmented calorimeter; Pure CsI scintillators; Detector calibration gain-matching and performance

¹ Corresponding author. Tel: +1-434-924-6786; fax: +1-434-924-4576.
E-mail address: frlez@virginia.edu (E. Frlež).

1 Introduction

The PIBETA detector [1] was built at the Paul Scherrer Institute [2] for the precise measurement of the branching ratio of the pion beta decay $\pi^+ \rightarrow \pi^0 e^+ \nu_e$ as well as several other rare pion and muon decays [3]. During the production runs in 1999-2001 and 2004, we collected a large data sample of pion and muon decay events corresponding to a total of 2.37×10^{13} pion stops, with stopping rates ranging between $5 \times 10^4 \pi^+/\text{s}$ and $1 \times 10^6 \pi^+/\text{s}$ [4–6].

In this paper we describe the computer-controlled gain-matching procedure used for the PIBETA calorimeter modules. The procedure was an essential component of an almost complete experiment automation, enabling our detector to run virtually free of human intervention for long periods of time.

Several systems have been used over the years for calibration and gain monitoring of detectors based on photomultiplier tubes (PMT) [7–17]. A majority of experiments use artificial light sources for a fixed energy reference, such as lasers or LED pulses. The reference signals are usually interfaced to the individual detectors via optical fibers. An alternative approach uses laser light to excite a single Plexiglas plate integrated within a calorimeter box, obviating the need for individual fiber couplings [18–20].

We have chosen to rely on the comparison between measured and simulated energy spectra of weak pion and muon decays in order to provide fixed energy references for the gain factors and applied high voltage settings of individual detectors. We have used both continuous energy spectra having a well defined end-point, such as the Michel decay of the muon, $\mu^+ \rightarrow e^+ \nu \bar{\nu}$, with maximum positron energy of $m_{\mu^\pm}/2 = 52.8 \text{ MeV}$, as well as the mono-energetic 69.8 MeV positron peak of the rare $\pi^+ \rightarrow e^+ \nu$ decay, also designated as π_{e2} decay. These energy scales, utilized in automatic gain-matches, were cross-checked offline for consistency with the 135.0 MeV energy peak position of reconstructed neutral pions from the π_β decay.

This article contains the following discussions: in Section 2 we briefly describe the general design of the PIBETA detector. The pure CsI calorimeter, the most important part of the detector, is described in more detail in Sec. 3. Section 4 deals with the calorimeter PMT's and associated voltage dividers, custom-made for this experiment to insure the required linearity of response and the large dynamical range. The main subject of this article, the flexible gain-matching procedure, is covered in Sec. 5. Several gain-matching examples from the PIBETA production runs are presented in its subsections. The temperature dependence of the calorimeter analog to digital converter (ADC) spectra is illustrated in Sec. 6. The resulting calorimeter energy resolution and the PMT gain stability are discussed in Sec. 7. We close with the summary of

the main points and advantages of our gain-matching procedure.

2 PIBETA detector

The PIBETA apparatus is a large solid angle non-magnetic detector optimized for measurements of photons and electrons in the energy range of 5–100 MeV. The main sensitive components of the apparatus, shown and labeled in Fig. 1, are:

- (1) a thin forward beam counter BC, two cylindrical active collimators AC_1 and AC_2 , and an active degrader AD, all made of plastic scintillators, used for the beam definition;
- (2) a segmented active plastic scintillator target AT, used to stop the beam particles and sample lateral beam profiles;
- (3) two concentric low-mass cylindrical multi-wire proportional chambers $MWPC_1$ and $MWPC_2$ for charged particle tracking, surrounding the active target;
- (4) a segmented fast plastic scintillator hodoscope PV, surrounding the $MWPC$'s, used for particle identification;
- (5) a segmented fast CsI shower calorimeter, surrounding the target region and tracking detectors in a near-spherical geometry;
- (6) cosmic muon plastic scintillator veto counters CV around the entire apparatus (not shown).

All above detector components, together with the delay cables for analog signals from photomultiplier tubes, high voltage (HV) power supplies, MWPC instrumentation and gas system, fast trigger electronics, two front end computers for data acquisition and slow control system are mounted on a single platform and can be moved as a single unit into the experimental area. After the detector platform is precisely positioned with respect to the beam line, providing the electrical power and Ethernet connections makes the detector operational in less than 24 hours.

3 PIBETA calorimeter

The central part of the PIBETA detector is the electromagnetic shower calorimeter, shown in Fig. 2. The calorimeter's nearly spherical geometry is

obtained by the ten-frequency class II geodesic triangulation of an icosahedron [21]. Its active volume is made of pure CsI [22–24].

The calorimeter consists of 240 pure CsI crystals. The chosen geodesic division results in 220 truncated hexagonal and pentagonal pyramids covering the total solid angle of $0.77 \times 4\pi$ sr. An additional 20 veto crystals line two detector openings for beam entry and detector readout, and act as electromagnetic shower leakage vetoes. The inner radius of the calorimeter is 26 cm, and the radial module length is 22 cm, corresponding to 12 CsI radiation lengths ($X_0=1.85$ cm [25]). There are nine different module shapes: four irregular hexagonal truncated pyramids (we label them HEX–A, HEX–B, HEX–C, and HEX–D), one regular pentagon (PENT), and two irregular half-hexagonal truncated pyramids (HEX–D1 and HEX–D2), plus two trapezohedrons which serve as calorimeter vetoes (VET–1 and VET–2). The CsI module volumes vary from 797 cm^3 (HEX–D1/2) to 1718 cm^3 (HEX–C).

All CsI crystal surfaces were polished and hand-painted with a special organo-silicon mixture in order to optimize the light collection and minimize surface deterioration [26].

The average scintillation light yield of the CsI detectors measured in a dedicated apparatus was 62 photoelectrons/MeV at the ambient temperature of 18°C . The average single CsI detector timing uncertainty was determined to be 0.68 ns rms. The temperature coefficient of the light output extracted from cosmic muon measurements was $-1.56 \text{ \%}/^\circ\text{C}$ [27,28].

4 Photomultiplier tubes, voltage dividers, and high voltage supplies

Electron Tubes (ET, formerly EMI) 9821QKB 10-stage fast PMT’s [29] with $\varnothing 75$ mm end windows were glued to the back faces of the hexagonal and pentagonal CsI crystals using a $300 \mu\text{m}$ layer of Sylgard 184 silicone elastomer (Dow Corning RTV silicon rubber plus catalyst). The smaller half-hexagonal and trapezoidal detector modules were equipped with $\varnothing 46$ mm 10-stage ET/EMI 9211QKA PMT’s [29]. Both types of PMT have quartz windows transparent to light with wavelengths down to 175 nm. The window transparency peaks near ~ 380 nm [29] and is therefore approximately matched to the spectral excitation of the pure CsI fast scintillation light component, which has maximum room temperature emission near ~ 310 nm [30].

The PMT high voltage dividers, designed and built at the University of Virginia, were based on an ET-recommended circuit. The dividers reduce the

so-called “super-linearity” exhibited by many PMT’s well below the onset of saturation ($> 50 \mu\text{A}$) by minimizing the ratio of anode current to resistor string current with adequately sized capacitors on the last few dynodes and through use of active circuit elements. The diagram of the voltage divider circuit is shown in Fig. 3.

We have chosen the SbCs dynodes offered by ET to suppress the dynode material-dependent PMT gain shift that occurs at small anode currents (1–10 μA). The maximum PMT non-linearity measured in a test with a pair of light-emitting diodes was less than 2% over the full dynamic range expected in the π_β decay rate measurement [31].

Two LeCroy 1440 high voltage mainframes provided the high voltage for all PMT’s. This 340-channel HV system had computer control capability and thus allowed for frequent, remote changes in the HV supplied to the PMT’s. The demand HV values could be set in 1 V increments with an accuracy and reproducibility of $\simeq 1$ V, which corresponded to a gain change of $\sim 0.5\%$ for our CsI detector PMT’s operating in the range of 1500 V to 2200 V.

5 Gain-matching procedure

5.1 Calorimeter energy clustering and clumping

Energies deposited by charged and neutral particles in the calorimeter are used not only to measure the energy of the traversing particle but also to define a basic element of the PIBETA detector trigger logic. Therefore, the signal coming from the calorimeter PMT’s was split into two branches, namely a “trigger” branch which supplied the signal for the trigger logic and the analog “signal” branch at the input of the digitizing FASTBUS ADC’s. In order to obtain the best possible performance in both branches we should consider the following characteristics of the calorimeter response to 65–70 MeV photons from π_β decay at rest and 69.8 MeV positrons from $\pi^+ \rightarrow e^+\nu$ decay process:

- (1) Electromagnetic shower profiles of the mean deposited energies are similar for photons and positrons, in particular for $\theta_c \geq 12^\circ$, with θ_c being the half-angle of a conical bin concentric with the direction of an incident particle.
- (2) A group of 9 detectors (a CsI “cluster”) constitutes an excellent summed energy trigger as it registers on average $\geq 98\%$ of the incident particle energy.

- (3) In case of a non-central hit, the sum of the energies in the crystal with the most deposited energy and its nearest neighbors contains 90 % of the entire calorimeter energy.

The summing and discrimination of the analog CsI “cluster” pulses in the trigger branch was done in dedicated linear summer/discriminator modules. The logic signal outputs of these custom made single-width NIM UVA125 summer/discriminator units provided the basic building blocks for more complex physics triggers.

To analyze an acquired event we make use of signal-branch ADC and TDC values recorded for “clumps,” CsI detector groupings consisting of the centrally hit crystal and its nearest neighbors. The initial inspiration for our algorithm was the Crystal Ball detector idea of “a clump discriminator function” [32]. The cluster-finding algorithm operates in the on-line analyzer program and identifies calorimeter shower clumps due to the interaction of a single ionizing particle. The algorithm first constructs a list of up to 6 nonadjacent calorimeter modules in order of decreasing deposited energy (“clump centers”). The minimum calibrated energy allowed for a clump center is 1.0 MeV, which is lower than the low energy discriminator threshold (LT) of $\simeq 4.5$ MeV. The clump energies are next calculated by adding the energies of neighboring modules to the energy recorded in the clump center, provided that, the TDC hit values of the neighbors fall within a specified time window of 10 ns. Energies of crystals outside that time window are not included in the energy sum, as they are assumed to be related to accidental coincidences. The number of nearest neighbors varies from 5 for a centrally hit pentagon, to 7 neighbors for the outlying HEX-C modules. The time associated with a clump is calculated as the energy-weighted average of all clump members. The clumping algorithm finally saves summed energies, times and the relative angles between all clump pairs and these clump sums are used in the gain matching process.

Hence, energy calibration of the PIBETA calorimeter involves two correlated processes: (1) equalizing the response of 220 trigger-defining non-veto CsI detector signals to a common UVA125 discriminator threshold by means of adjusting high voltages applied to individual CsI PMT’s, and (2) calibrating analog signal gains of 220 non-veto CsI detectors to achieve best possible energy resolution in the signal branch, by introducing 220 software gain factors for individual detectors. The need for the software gains arises from the relative difference between the signal amplitudes of an individual CsI detector at the trigger branch and at the signal branch due to different signal attenuation in the delay cables of two branches, differences in the resistor values in passive signal splitters and/or small mis-matches in time offsets of the two branches. These two adjustments can be done both manually by the experiment operators, as well as automatically by a computer program.

5.2 Threshold-matching CsI detectors

As explained above, the first step in the gain equalization of the CsI detectors requires the matching of energy-equivalent discriminator thresholds of the individual modules. For that purpose we have used $\pi^+ \rightarrow e^+\nu$ events collected with the one-arm high threshold (HT) trigger set at $\simeq 54$ MeV. We defined an on-line one-dimensional 240-bin histogram for the indices of the individual CsI detectors that were hit in an event. For every identified positron track the histogram was filled with an index of the CsI clump center (detector receiving the maximum energy deposition). Ideally, for perfectly threshold-matched detectors the resulting histogram shape would reflect the solid angle covered by each detector. Detector HV's are therefore adjusted remotely via computer in an iterative process until the threshold histogram shape matches the detector yields predicted in a Monte Carlo simulation.

An example of four consecutive iterations in the threshold-matching process is shown in Fig. 4. At the end of the process the HV's of the detectors were required to change by less than 1 V on average. That operation fixed all CsI discriminator thresholds, expressed in absolute MeV-equivalent units, at the same energy value (usually within 0.5 %, corresponding to ± 1 V in PMT HV).

5.3 Gain-matching with $\pi^+ \rightarrow e^+\nu$ peaks and Michel edge spectra

The software gain multipliers which optimize the energy resolution of the digitized ADC spectra can be determined once the discriminator thresholds are equalized at the trigger branch by adjusting the PMT high voltages. For a detector equipped with an n -stage PMT, a normalized gain change g , relating two different gain settings 1 and 2, depends on the ratio of the software gains s_i and the corresponding high voltages V_i :

$$g = \frac{s_1}{s_2} \cdot \left(\frac{V_1}{V_2} \right)^m, \quad (1)$$

where m is an exponent close to n , the number of the PMT stages. Parameter m depends on the design of the PMT used, as well as on its voltage divider. The above equation gives the real gain of a scintillator detector at the setting 2, related to the gain at setting 1. The actual detected energies E_i are then calculated from the raw ADC_i values:

$$E_i(\text{MeV}) = s_i \cdot ADC_i. \quad (2)$$

Figure 5 represents the gain measurements of a representative CsI detector as a function of the high voltage applied to its PMT. The fitted coefficient m is equal to 9, consistent with the expectation for a 10-stage photomultiplier. The distribution of the gain exponents for a large subset of the CsI detectors is shown in Fig. 6. The average value of the parameter m is 9.4 with the rms spread of 1.4 units.

As indicated in the Introduction, we have used both (i) the continuous $\mu^+ \rightarrow e^+\nu\bar{\nu}$ (Michel) positron spectrum, and (ii) the mono-energetic π_{e2} peak in order to determine the HV change and software gain change applied to each CsI module. In Fig. 7 we show the GEANT3 [33] Monte Carlo simulation of the full Michel energy spectrum taken with the low threshold trigger (top panel) and the π_{e2} positron recorded with the high threshold trigger (middle panel). The MC simulation reflects a realistic and detailed description of the PIBETA detector response. Mixing both energy distributions with the $\pi^+ \rightarrow e^+\nu$ branching ratio and simulating the realistic high threshold trigger produces the bottom panel of Fig. 7. The high voltage settings of all CsI detectors can be scaled simultaneously by a common factor. The effect of the overall HV re-scaling on our energy spectra is demonstrated in three panels of Fig. 8. Similar picture is observed for the energy spectrum in a clump centered around any given non-veto crystal. Therefore, such a combined positron spectrum in the HT trigger can be used for the in situ gain-matching of the entire CsI calorimeter. For the well-matched HT trigger the Michel-edge-to- $\pi^+ \rightarrow e^+\nu$ peaks ratio was empirically fixed to be three-to-one. Keeping this ratio a constant provides continuous monitoring of the trigger threshold, while the precise position of the π_{e2} decay positron energy peak determines the value of the software gains to be applied to the individual crystals.

The MIDAS data acquisition system used in the experiment incorporates an integrated slow control system with a fast on-line database (ODB) and a history system [34]. Values of the software gains s_i (all initially set to 1.0) are kept in the on-line experiment database in the global memory section accessible to all running processes. If automatic gain-matching is enabled by setting the corresponding ODB flag, counting statistics in the 220 energy clump histograms are checked at the end of every run. For the histograms with integrated event counts exceeding the pre-set minimum yield of 1,000 events, the π_{e2} and Michel edge peaks are simultaneously fitted with a double Gaussian function. The example of such a fit for four representative CsI detectors (PENT 8, HEX-A 45, HEX-C 130, and HEX-D 190) is shown in Fig. 9.

Once at least 210 histograms have successful fits, the fit results are used to calculate new values of software gains and to rewrite the old values in the on-line database. The two-dimensional CsI energy histogram shown in Fig. 10 was used during routine gain monitoring. The CsI detector index is displayed along the vertical histogram axis, enabling a shift taker to notice easily the

detectors whose Michel edges and π_{e2} peaks are out of alignment. At the end of each gain matching iteration, a log file documenting the Gaussian fits was generated automatically and submitted to the electronic logbook. The head portion of that log file looks like this:

```

0 N=1254 C2=3.377 CM=54.73 WM= 3.62 C=67.55 W=10.05 G=0.997 +- 0.001 R=0.242 HV=-1
1 N=1100 C2=2.781 CM=53.95 WM= 4.24 C=66.51 W= 9.69 G=1.007 +- 0.001 R=0.307 HV=+0
2 N=1178 C2=2.825 CM=54.94 WM= 4.70 C=66.37 W=10.94 G=1.009 +- 0.002 R=0.305 HV=+0
3 N=1261 C2=3.333 CM=54.22 WM= 4.95 C=66.61 W=11.75 G=1.006 +- 0.002 R=0.338 HV=+0
4 N=1149 C2=3.118 CM=53.91 WM= 4.23 C=66.23 W= 9.84 G=1.017 +- 0.002 R=0.267 HV=-1
5 N=1226 C2=2.763 CM=52.89 WM= 4.05 C=66.91 W= 8.90 G=1.001 +- 0.001 R=0.301 HV=+0
6 N=1174 C2=2.485 CM=54.25 WM= 5.30 C=67.55 W= 9.64 G=0.987 +- 0.001 R=0.375 HV=+1
...

```

The first column in the above list is the detector number, followed by the integrated event count, and the six fitted parameters. As described above, the change of the software gain g in the eighth column is calculated from the deviation of the second fitted peak C from the preset target value. The last two items are R , a parameter proportional to the χ^2 of the fit, and the calculated PMT HV change applied in order to keep the Michel-edge-to- π_{e2} peaks ratio fixed. Only a few software gain iterations were necessary to attain nearly optimal energy resolution of the calorimeter. In Fig. 11 we show the one-arm calorimeter energy spectrum at the start of the measurement and the improvement in the resolution following the two passes of software gain changes.

6 Temperature dependence of light output

The photoelectron statistics in the CsI crystals and resulting gain and energy resolution of the CsI detector are highly dependent on the ambient temperature, making it imperative to maintain the temperature as stable as possible. Additionally, CsI is a hygroscopic compound whose optical properties are degraded by absorbed moisture. The design goals for the temperature stabilization system were to maintain:

- (1) constant CsI calorimeter temperature of 22° C, stable to $\pm 0.02^\circ$ C, ensuring gain stability of ± 0.02 MeV at 70 MeV;
- (2) relative humidity inside the detector thermal housing $\leq 50\%$.

The PIBETA calorimeter is enclosed in a thermal housing lined with five 4 cm thick Styrodur panels with a low heat conductivity. A recirculating chiller unit uses water as a cooling fluid and maintains the temperature constant within 0.02° C. During detector operation two heater/fan units in the air pipes next to the cooling heat exchanger are used in a feedback loop to regulate the air temperature to within 0.02° C. The air temperature is measured just after

both heaters, and the average CsI calorimeter temperature is determined using eight sensors distributed uniformly around the CsI sphere.

Figure 12 shows the variation of the CsI light output caused by one instance of a failure of the detector temperature control system. The three panels show that Michel edges and π_{e2} peak positions scale down with rising temperature in the absence of gain matching. Alternatively, these results indicate that the absolute energy threshold, expressed in MeV, is proportional to the temperature. The average CsI temperature coefficient extracted from the 2004 data set (panel 4 of Fig. 12) was $(-1.9 \pm 0.3)\%/^{\circ}\text{C}$, consistent with our earlier (1997-1999) measurements [27,28].

7 Calorimeter energy resolution and gain stability

Consistent applications of the gain stabilization procedures described in the preceding sections provide very stable response of the calorimeter over long periods of operation, as illustrated in Fig. 13. The top panel shows the run-to-run values for the fitted π_{e2} peaks for one representative 2 month period. The bottom panel displays the associated rms of the Gaussian fit for the upper part of the π_{e2} energy line-shape. The peak position was stable within $\pm 0.2\text{ MeV}$. While gain-matching was done manually in the set-up stages of the experiment, the subsequent runs achieve better energy resolution thanks to computer-controlled detector operation and lower beam stopping rate.

The peak $\pi^+ \rightarrow e^+\nu_e$ positron energy in CsI is affected by energy losses in the active target, plastic veto scintillator, and in the insensitive layers in front of the CsI crystals, positron annihilation losses, photoelectron statistics of individual CsI modules, and axial and transverse coefficients parameterizing the nonuniformities of CsI light collection. Overall, the π_{e2} peak position was measured with absolute accuracy of $\pm 0.03\text{ MeV}$. The best achieved rms fractional resolution $\Delta E/E$ was 4.5% at 67 MeV. Contributions from the photoelectron statistics and the light collection nonuniformities produce an rms of 3.6%, while the gain matching uncertainty adds an additional rms of 2.6%.

8 Results and conclusions

We have designed an in situ computer-controlled system for the gain control of the PIBETA modular CsI electromagnetic calorimeter. We have used the high-

energy edge of the Michel spectrum as well as the mono-energetic $\pi^+ \rightarrow e^+\nu$ positron peak as the reference points. The computer program running at the end of each run adjusted the PMT high voltages and/or the software gain factors in order to compensate for the gain drifts and the slow continuous gain decrease due to the CsI radiation damage and aging. The system has successfully matched the detector gains and controlled individual detector HV settings in the long term, virtually free of human intervention, maintaining the calorimeter rms energy resolution for 69.8 MeV decay positrons at $\Delta E/E \simeq 4.5\%$.

9 Acknowledgments

This work is supported and made possible by grants from the US National Science Foundation and the Paul Scherrer Institute.

References

- [1] E. Frlež, D. Počanić, K. A. Assamagan et al., Nucl. Instrum. & Meth. A 526 (2004) 300.
- [2] PSI Users' Guide: Accelerators Facilities (Paul Scherrer Institute, Villigen PSI, 1994).
- [3] D. Počanić, K. A. Assamagan, J. P.Chen et al., A Proposal for a Precise Measurement of the $\pi^+ \rightarrow \pi^0 e^+ \nu$ Decay Rate (PSI R-89.01) (Paul Scherrer Institute, Villigen, 1991).
- [4] D. Počanić, E. Frlež, V.A. Baranov et al., Phys. Rev. Lett. 93 (2004) 181803-1-4.
- [5] E. Frlež, D. Počanić, V.A. Baranov et al., Phys. Rev. Lett. 93 (2004) 181804-1-4.
- [6] M. Bychkov, D. Počanić et al., arXiv:0804.1815
- [7] J. Berger et al., Nucl. Instr. and Meth. A 279 (1989) 343.
- [8] S. Bianco et al., Nucl. Instr. and Meth. A 482 (1991) 48.
- [9] J. W. Mitchel et al., Nucl. Phys. Proc. Suppl. 32 (1993) 106.
- [10] J. Zabierowski et al., Nucl. Instr. and Meth. A 338 (1994) 577.
- [11] T. Hehl et al., Nucl. Instr. and Meth. A 354 (1995) 505.
- [12] T. Peitzmann et al., Nucl. Instr. and Meth. A 376 (1996) 368.
- [13] P. Adamson et al., Nucl. Instr. and Meth. A 492 (2002) 325.
- [14] D. Hanna et al., Nucl. Instr. and Meth. A 482 (2002) 271.
- [15] H. Tanaka et al., Nucl. Instr. and Meth. A 515 (2003) 725.
- [16] V.A. Batarin et al., Nucl. Instr. and Meth. A 534 (2004) 486.
- [17] V.A. Batarin et al., Nucl. Instr. and Meth. A 556 (2006) 94.
- [18] B. B. Brabson et. al., Nucl. Instrum. Meth. A 332 (1993) 419; R. R. Crittenden et al., Nucl. Instrum. Meth. A 387 (1997) 377.
- [19] E. Frlež, Fizika B 8 (1999) 29.
- [20] R. T. Jones et. al., Nucl. Instrum. Meth. A 570 (2007) 384.
- [21] H. Kenner, *Geodesic Math and How to Use It* (University of California Press, Berkeley, 1976).
- [22] H. Kobayashi, A. Konaka, K. Miyake et al., Kyoto University Preprint KUNS-900 (1987).
- [23] S. Kubota, H. Murakami, J. Z. Ruan et al., Nucl. Inst. and. Meth. A 273 (1988) 645.

- [24] S. Kubota, S. Sakuragi, S. Hashimoto et al., Nucl. Inst. and Meth. A 268 (1988) 275.
- [25] S. Eidelman et al., Phys. Lett. B592, 1 (2004). Latest WWW update accessible at <http://www-pdg.lbl.gov>.
- [26] V. I. Goriletsky, L. A. Andryuschenko, and A. M. Kudin, Private Communication, Alkali Halide Crystal Division, Institute for Single Crystals, National Academy of Sciences of Ukraine (60 Lenin Prosp., 310001 Kharkov, Ukraine).
- [27] E. Frlež, I. Supek, K. A. Assamagan et al., Nucl. Inst. and Meth. A 440 (2000) 57.
- [28] E. Frlež, Ch. Brönnimann, B. Krause et al., Nucl. Instr. and Meth. A 459 (2001) 426.
- [29] THORN-EMI Electron Tubes Catalog: *Photomultipliers and Accessories* (Rockaway, NJ, 1993).
- [30] C. L. Woody, P. W. Levy, J. A. Kierstead et al., IEEE Trans. Nucl. Sci. 37 (1990) 492.
- [31] L. C. Smith, *PMT Evaluation PIBETA Note*, accessible at URL <http://pibeta.phys.virginia.edu/~pibeta/>.
- [32] M. Oreglia, Ph. D. Thesis (Stanford University, SLAC-226, 1980).
- [33] R. Brun, F. Bruyant, M. Maire et al., GEANT 3.21 DD/EE/94-1 (CERN, Geneva, 1994).
- [34] S. Ritt, P.-A. Amaudruz et al., MIDAS Data Acquisition System, <http://midas.psi.ch/>.

Fig. 1. Schematic cross section of the PIBETA apparatus showing the main components: forward beam counter (BC), two active collimators (AC1, AC2), active degrader (AD), active target (AT), two MWPC's and their support, plastic scintillator charged particle veto detectors (PV) and PMT's, pure CsI calorimeter and PMT's.

Fig. 2. Panel (i): basic geometry of the pure CsI shower calorimeter. The sphere is made up of 240 elements, truncated hexagonal, pentagonal, and trapezoidal pyramids; it covers about 80% of 4π in solid angle. Panel (ii): an individual supercluster and its 5-supercluster complement. The PIBETA calorimeter comprises 10 minimally-overlapping superclusters.

Fig. 3. The PMT high voltage dividers, designed and built at the University of Virginia, are based on a modified ET/EMI-recommended circuit.

Fig. 4. Four consecutive iterations in the matching of CsI discriminator thresholds. Individual CsI detector HV settings were adjusted until the count rates of the positrons with energies exceeding ~ 50 MeV are roughly equalized. CsI veto detectors 220–239 were not included in the trigger.

Fig. 5. Dependence of an individual CsI detector's gain factor on the ET/EMI 9822QKB PMT high voltage. The LED signal level was adjusted to produce 700 pC at 2000 V.

Fig. 6. Distribution of slope coefficients for $\log(\text{HV})$ vs PMT gain for CsI detectors. The average fitted value of the coefficient was 9.4 for 10-stage PMT's.

Fig. 7. Monte Carlo simulation of the calorimeter response to (i) the continuous Michel positron energy spectrum with a theoretical end-point of 52.8 MeV (top), (ii) monoenergetic 69.8 MeV $\pi^+ \rightarrow e^+\nu$ energy spectrum (middle), and (iii) combined simulated ADC spectrum in the 1-arm high threshold trigger (bottom). The GEANT3 calculation used a realistic response of the CsI calorimeter.

Fig. 8. GEANT3 detector simulation: effects of a gain shift on the 1-arm low-threshold energy spectrum (top plot) and the resulting gain matched energy spectra for the 1-arm high-threshold trigger (bottom plots, after applying software gains).

Fig. 9. Typical individual double Gaussian fits of the Michel edge and π_{e2} peak for four different calibrated energy clump histograms.

Fig. 10. Composite two-dimensional online calorimeter energy spectrum for the one-arm high-threshold trigger. The abscissa represents CsI detector calibrated energy sum in MeV; the ordinate displays the clump sum index number from 0-239.

Fig. 11. Two iterations of gain-matching: measured positron ADC spectra acquired with the 1-arm high-threshold trigger. The positron energy represents a sum of pedestal-corrected ADC values for the centrally hit CsI detector and its nearest neighbors. The initial energy resolution of the $\pi \rightarrow e\nu$ peak is 8.0% rms, the final resolution is 4.9% rms.

Fig. 12. Dependence of the CsI detector gain factors on ambient temperature in the range 23.0 ± 1.2 degrees Celsius. The PIBETA detector is operated inside a temperature-controlled thermal enclosure.

Fig. 13. Long-term stability of the CsI online detector gains. The top panel shows the $\pi^+ \rightarrow e^+ \nu$ peak position for $\sim 2,000$ runs covering a two month period. The bottom panel represents the corresponding online peak resolution.

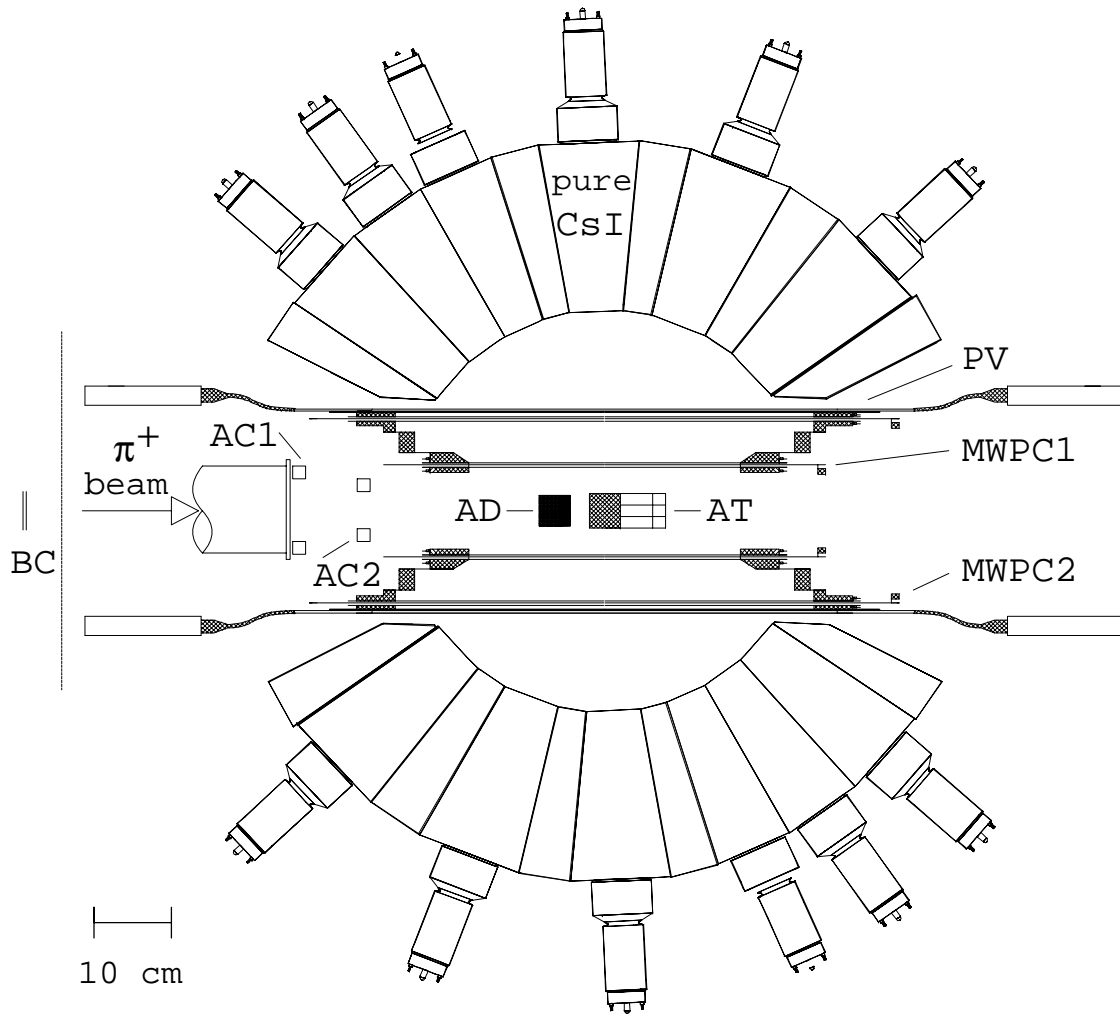
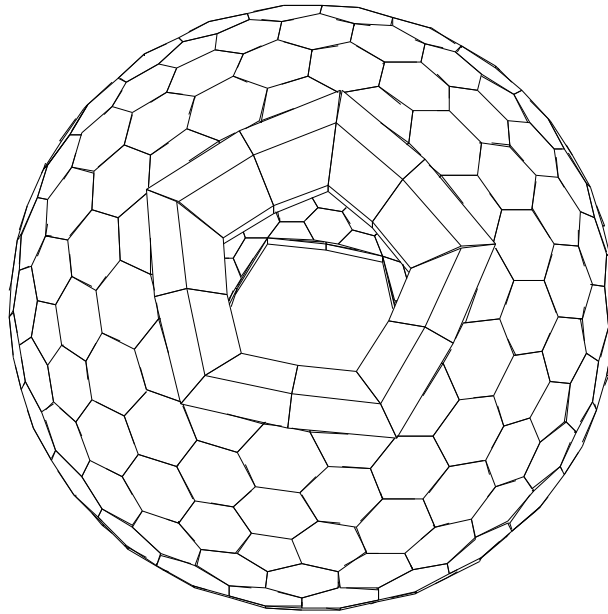
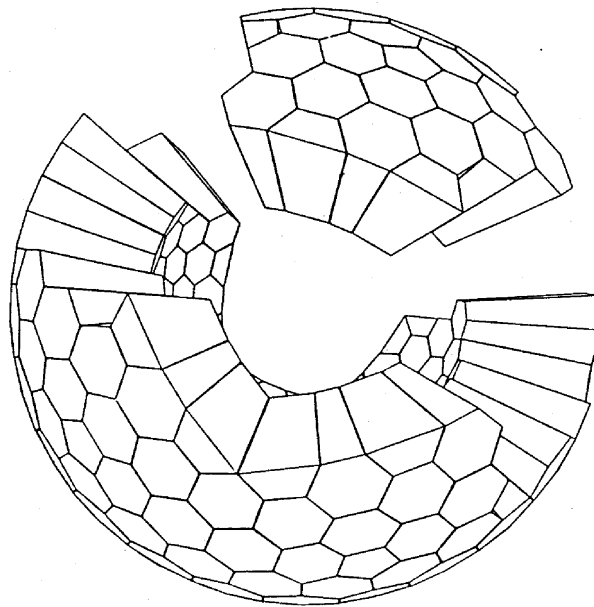


FIGURE 1



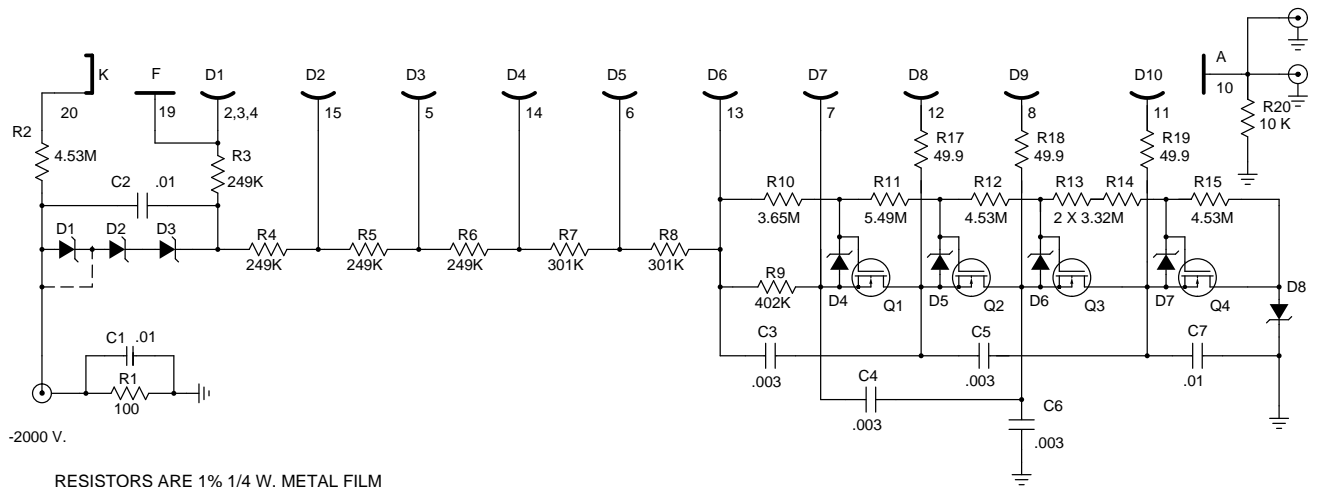
(i)



(ii)

FIGURE 2

UVA131 PHOTOMULTIPLIER BASE FOR EMI 9822(Q)KB OR = 9211(Q)KB (2")



RESISTORS ARE 1% 1/4 W. METAL FILM
 D1-D3 AND D8 ARE 1N989B 150V ZENERS
 REPLACE D1 WITH JUMPER FOR 9211 2" PMT
 D4-D7 ARE 1N751A 5.1V ZENERS
 Q1-4 ARE TYPE BSS125 600V MOSFETS

DIVIDER CURRENT IS 260 MICROAMPS. AT -1600 V.

FIGURE 3

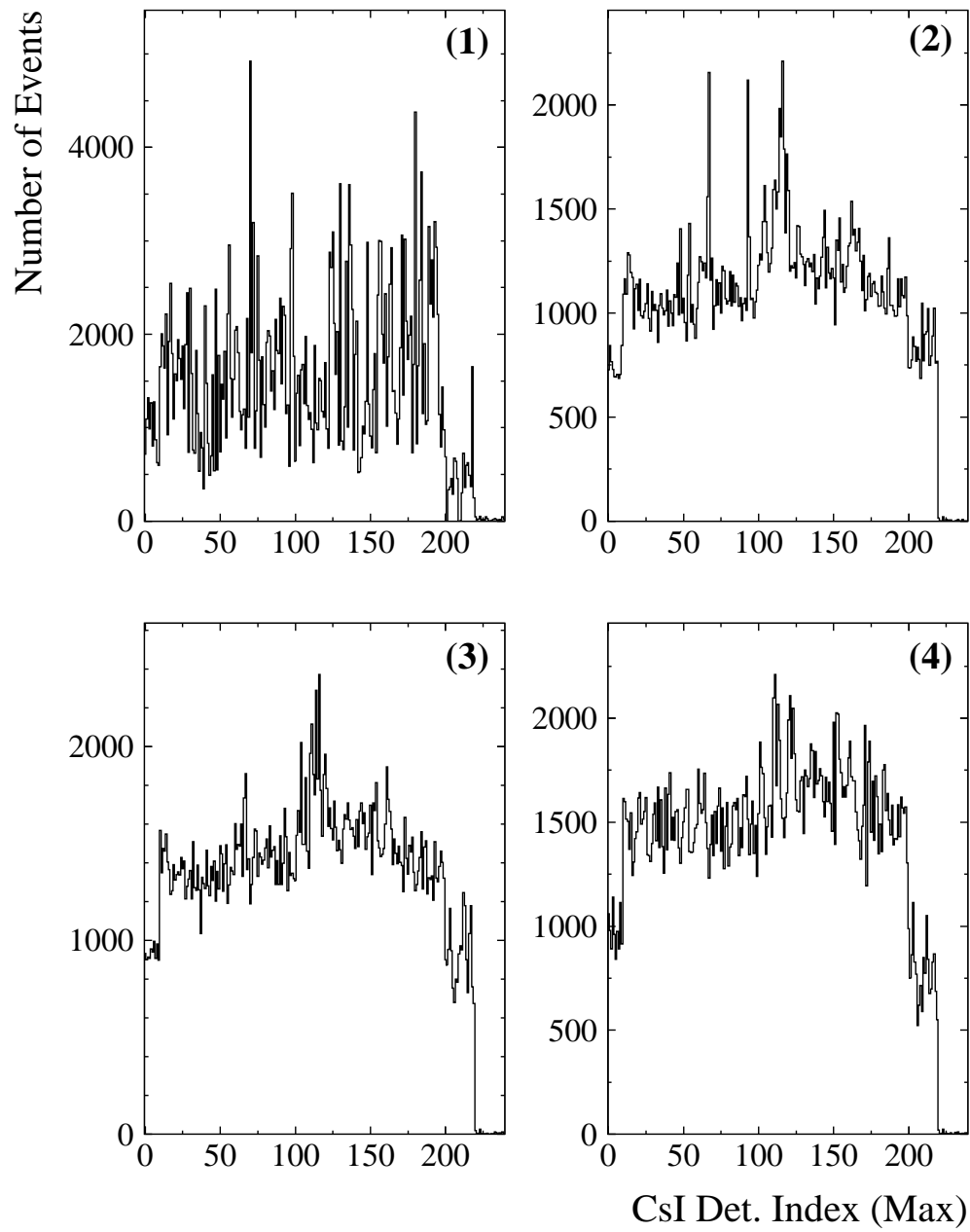


FIGURE 4

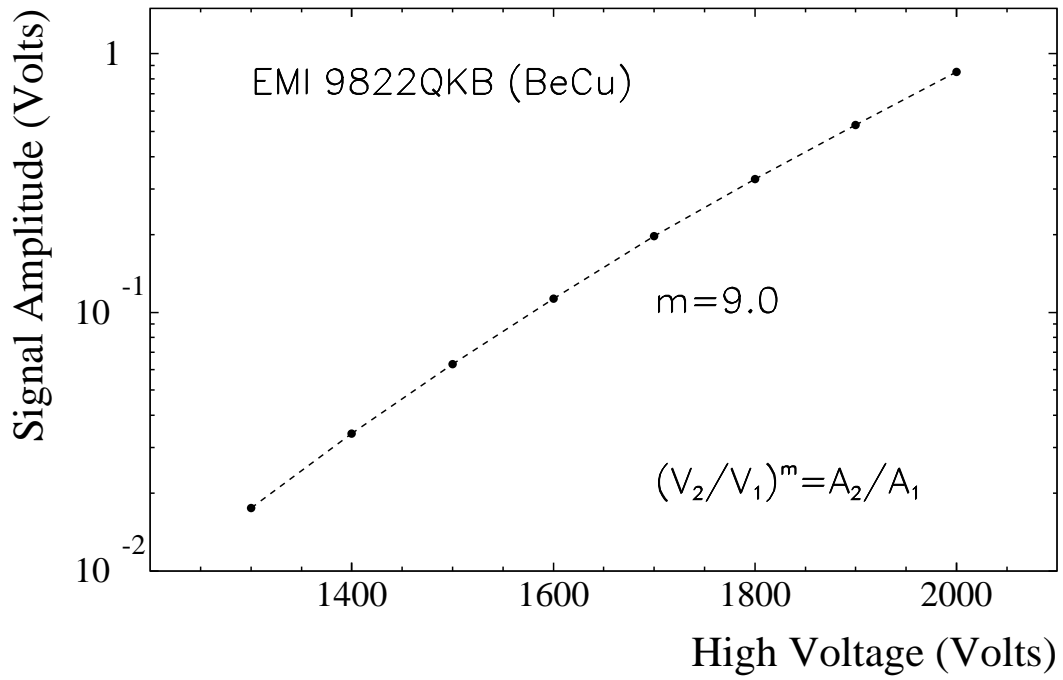


FIGURE 5

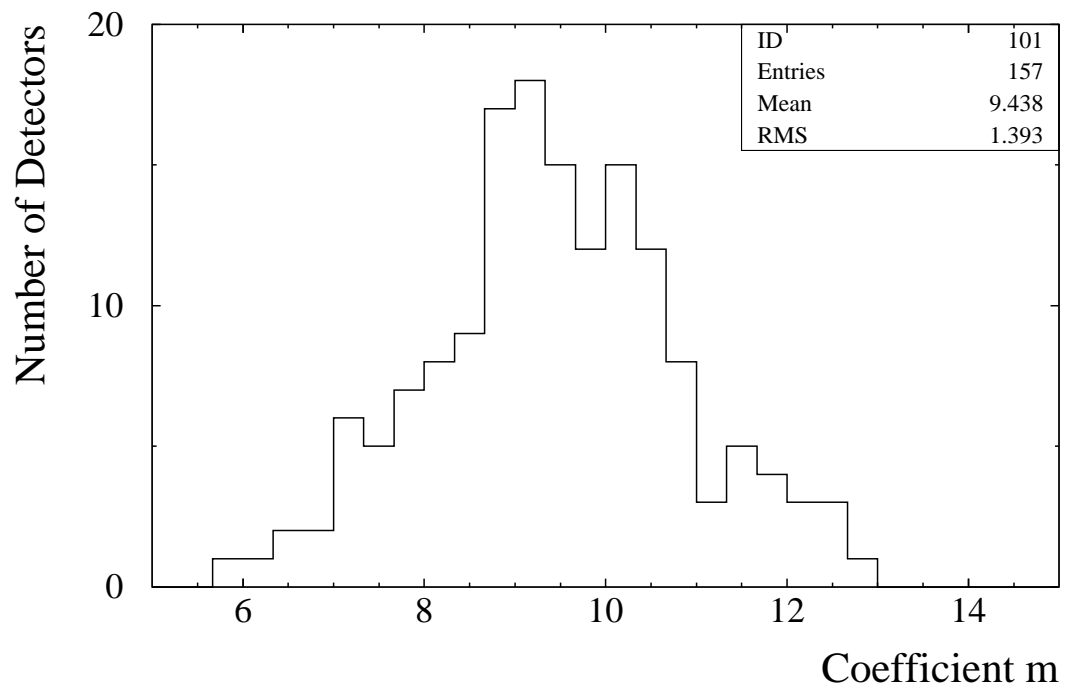


FIGURE 6

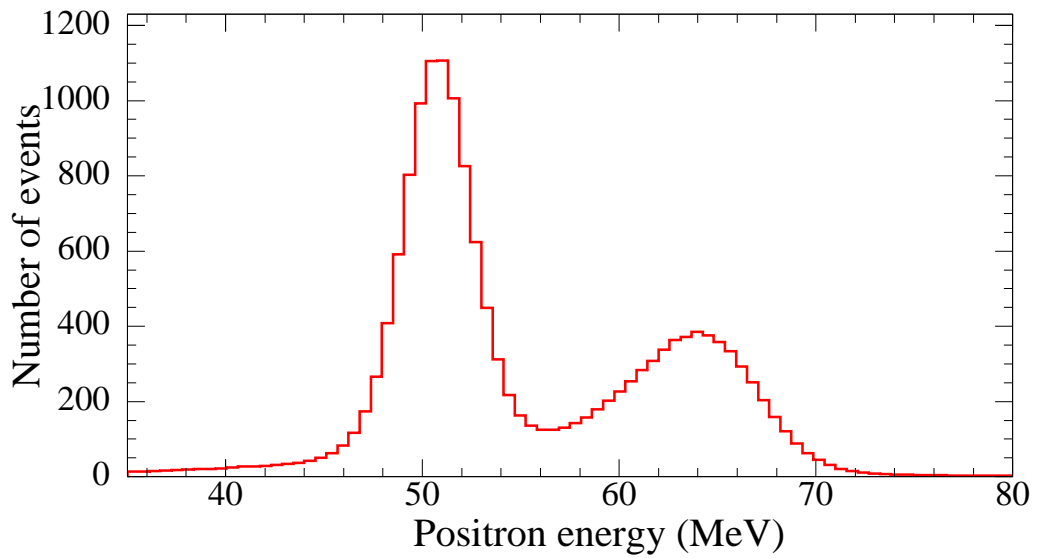
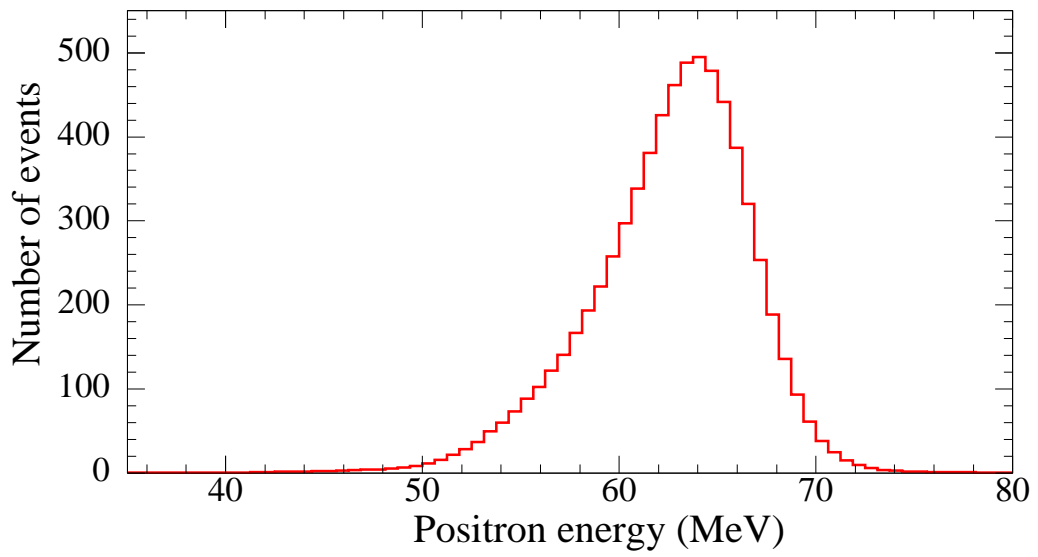
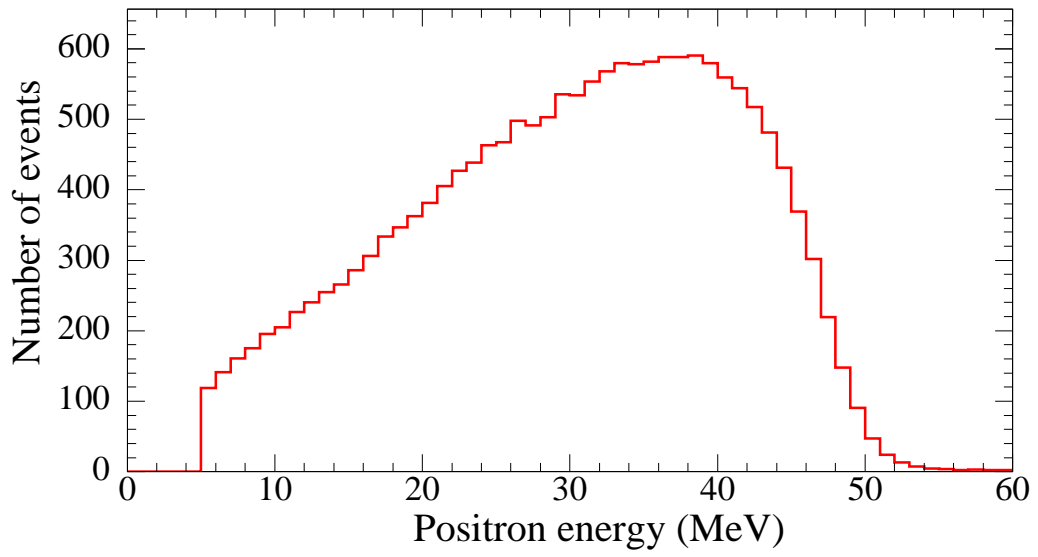


FIGURE 7

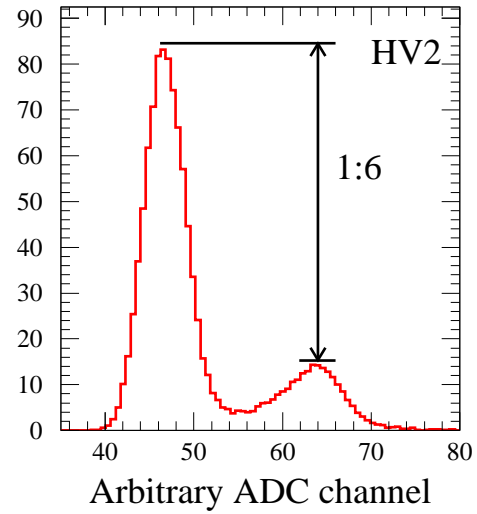
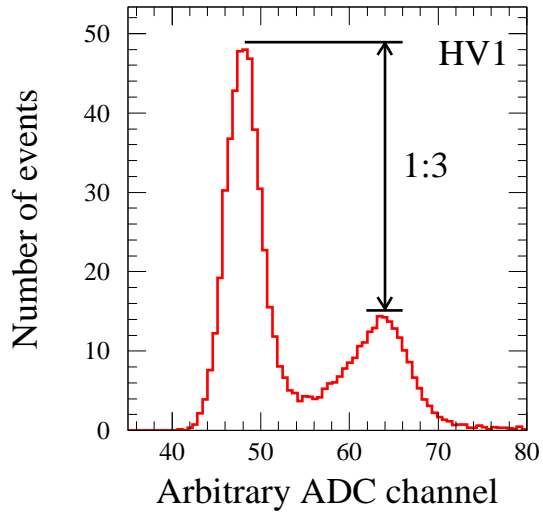
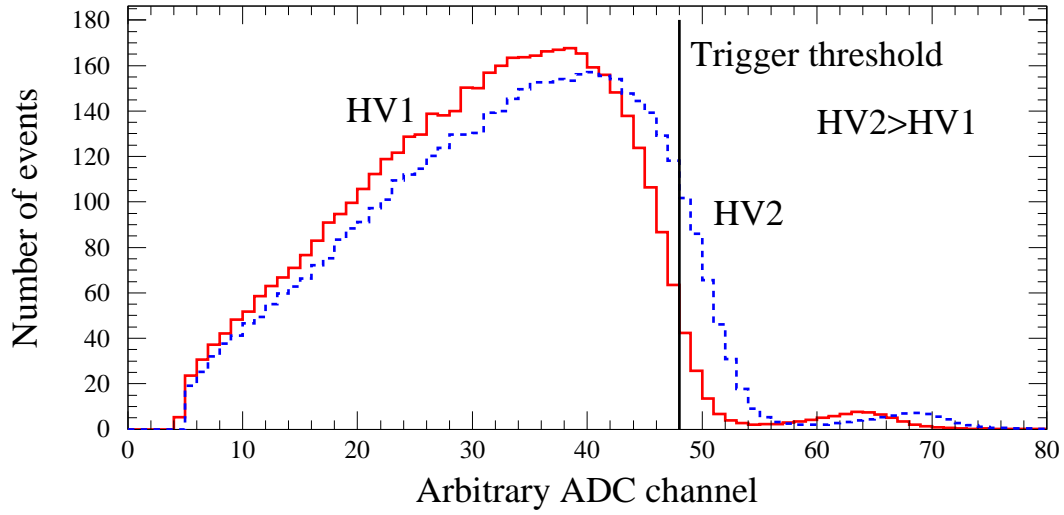


FIGURE 8

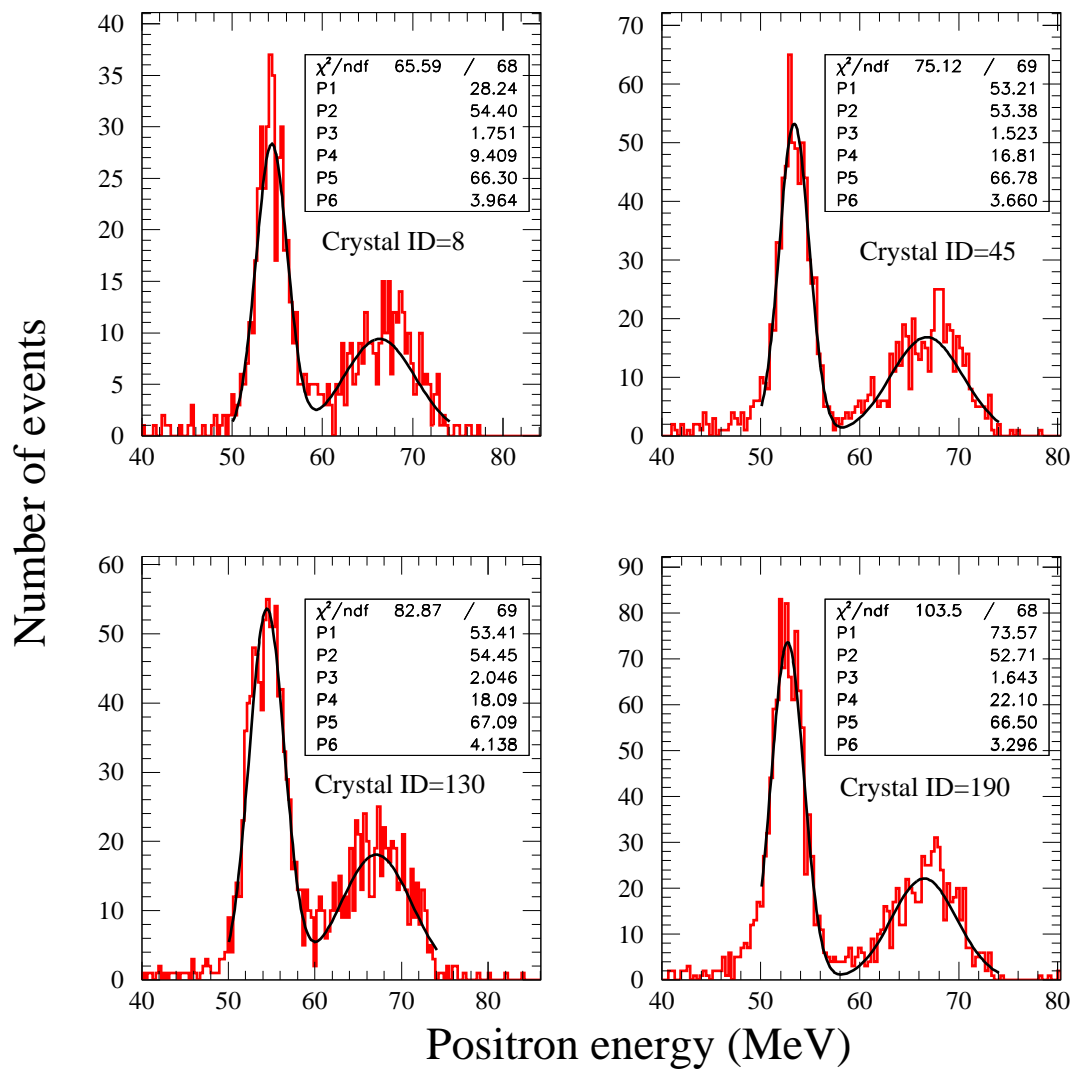


FIGURE 9

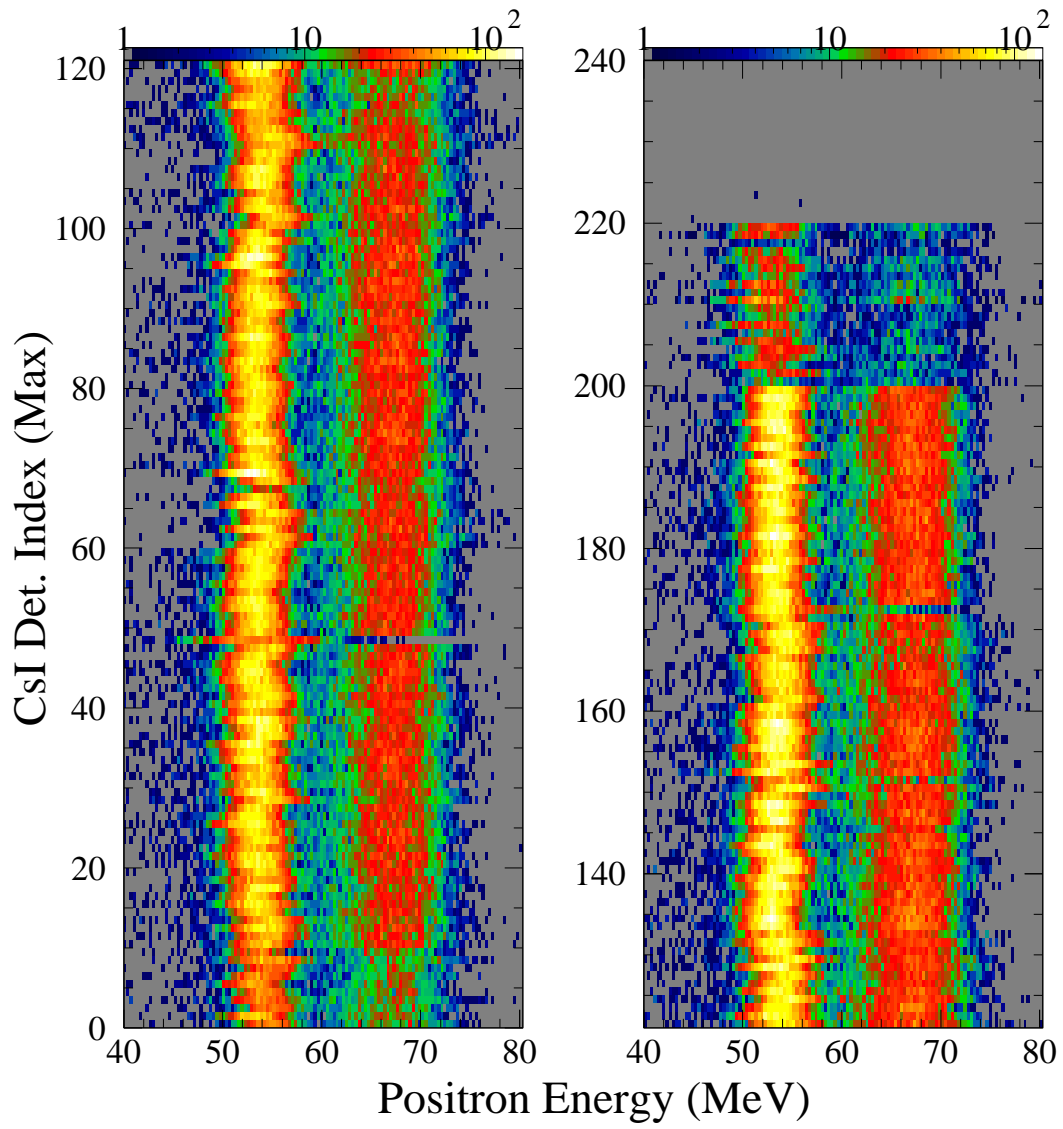


FIGURE 10

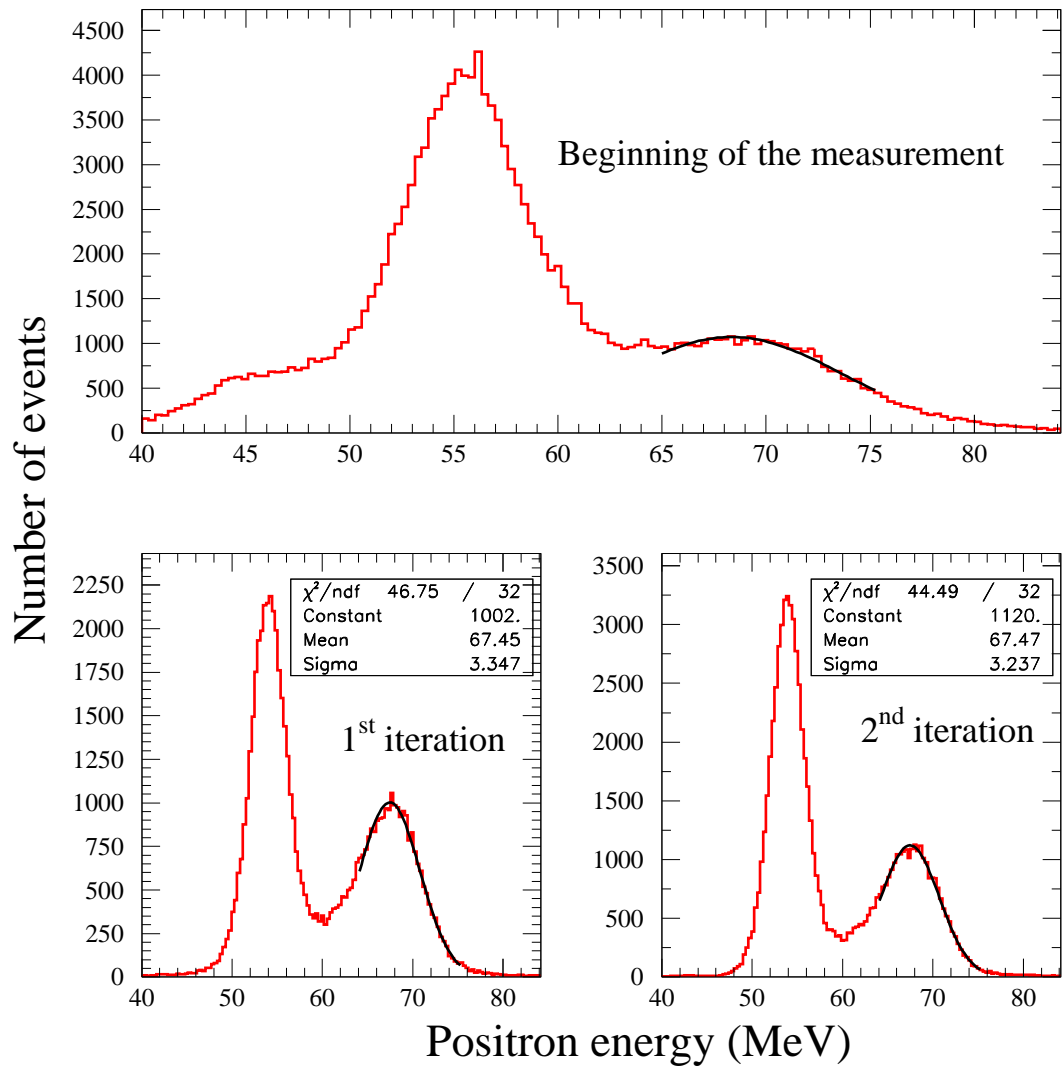


FIGURE 11

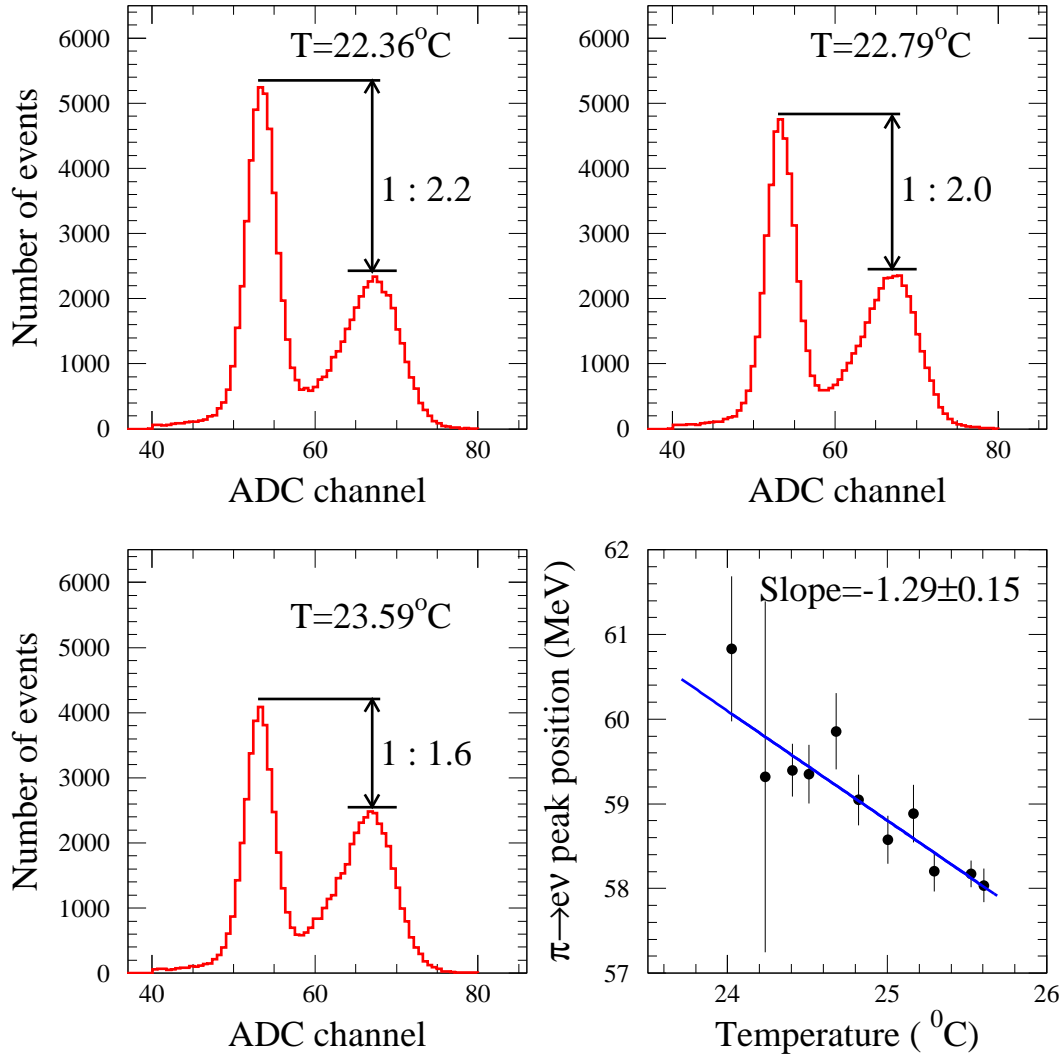


FIGURE 12

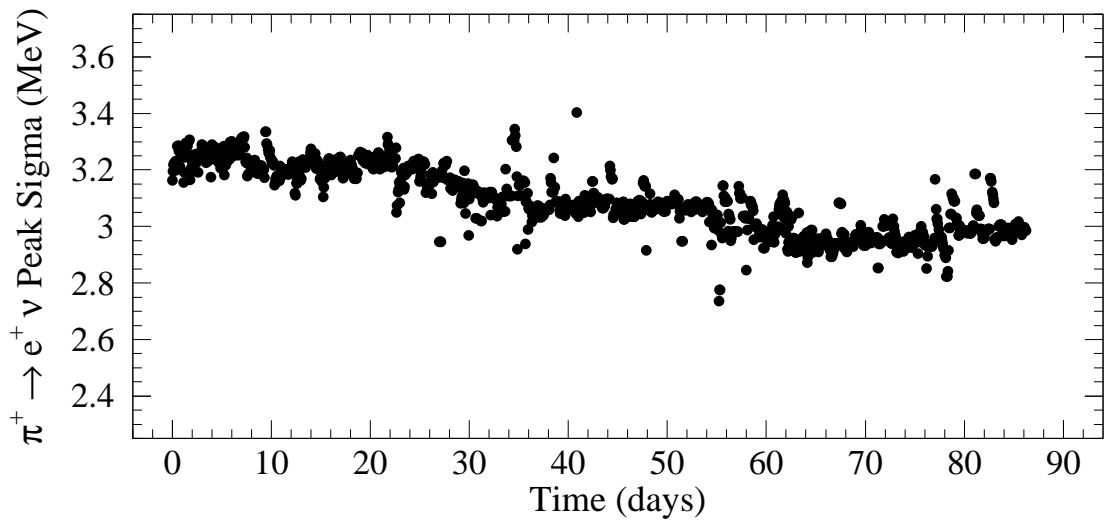
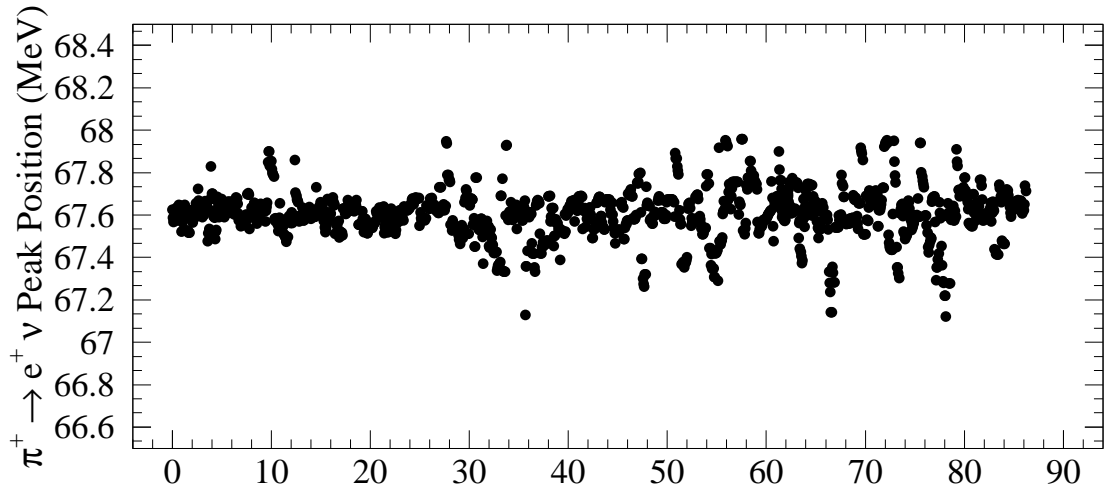


FIGURE 13

